Spectroscopy of ^{61}Fe via the neutron transfer reaction ^{2}H(^{60}Fe,p)^{61}Fe

S. Giron, F. Hammache, N. de Séréville, P. Roussel, J. Burgunder, M. Moukaddam, D. Beaumel, L. Caceres, G. Duchêne, E. Clément, et al.

Spectroscopy of ^{61}Fe via the neutron transfer reaction ^{2}H(^{60}Fe, p)^{61}Fe*

S. Giron,[1] F. Hammache,[1,*] N. de Séréville,[1] P. Roussel,[1] J. Burgunder,[2] M. Moukaddam,[3,†] D. Beaumel,[1] L. Caceres,[2] G. Duchêne,[3] E. Clément,[2] B. Fernandez-Dominguez,[2,‡] F. Flavigny,[1,4] G. de France,[2] S. Franchoo,[1] D. Galaviz-Redondo,[5] L. Gasques,[5] J. Gibelin,[6] A. Gillibert,[4] S. Grevy,[2,§] J. Guillot,[1] M. Heil,[7] J. Kiener,[8] V. Lapoux,[4] F. Maréchal,[1] A. Matta,[1,‖] I. Matea,[1] L. Nalpas,[4] J. Pancin,[2] L. Perrot,[1] A. Obertelli,[4] R. Raabe,[2,¶] J. A. Scarpaci,[1,#] K. Sieja,[3] O. Sorlin,[2] I. Stefan,[1] C. Stodel,[2] M. Takechi,[9] J. C. Thomas,[2] and Y. Togano[9]

[1]*Institut de Physique Nucléaire, CNRS-IN2P3, Université Paris-Sud, Université Paris-Saclay, 91406 Orsay Cedex, France*
[2]*GANIL, CEA/DRF-CNRS/IN2P3, B.P. 55027, F-14076 Caen Cedex 5, France*
[3]*IPHC, CNRS/IN2P3, Université de Strasbourg, F-67037 Strasbourg, France*
[4]*CEA, Centre de Saclay, IRFU/Service de Physique Nucléaire, F-91191 Gif-sur-Yvette, France*
[5]*Centro de Fisica Nuclear da Universidade de Lisboa, 1649-003 Lisboa, Portugal*
[6]*Normandie Université, ENSICAEN, UNICAEN, CNRS/IN2P3, LPC Caen, 14000 Caen, France*
[7]*GSI Helmholtzzentrum fur Schwerionenforschung GmbH, D-64291 Darmstadt, Germany*
[8]*CSNSM, IN2P3-CNRS, Université Paris-Sud, 91405 Orsay, France*
[9]*RIKEN Nishina Center, 2-1 Hirosawa, Wako, Saitama 351-0198, Japan*

(Received 28 December 2016; revised manuscript received 16 February 2017; published 31 March 2017)

The direct component of the ^{60}Fe$(n,\gamma)^{61}$Fe cross section was investigated by populating the bound states of the ^{61}Fe nucleus through the $(d,p\gamma)$ transfer reaction in inverse kinematics using a radioactive beam of ^{60}Fe at 27A MeV. The experiment was performed at GANIL using the MUST2 array and an annular double-sided silicon strip detector for the detection of the light charged particle in coincidence with the photons measured in the EXOGAM γ-ray detectors. For the first time, the spectroscopic factors of the first $3/2^-$, $5/2^-$, $1/2^-$, and $9/2^+$ states of ^{61}Fe were deduced experimentally from an adiabatic distorted wave approximation analysis of the data. The obtained results show a very good agreement with the shell-model predictions. The calculated direct component of the (n,γ) cross section was found negligible and of about 2% of the total, indicating a dominant resonant component.

DOI: 10.1103/PhysRevC.95.035806

I. INTRODUCTION

The radioactive isotope ^{60}Fe ($T_{1/2} = 2.2$ Myr [1]) plays an important role in astrophysics because its various observations shed light on topics such as massive star nucleosynthesis or the past and recent history of our solar system.

Observations of the sky in the MeV γ-ray band with the RHESSI [2] and INTEGRAL [3] spacecrafts have revealed a diffuse emission in the galactic plane at $E_\gamma = 1173$ and 1333 keV coming from ^{60}Co, the daughter nucleus of ^{60}Fe. These observations point out that ongoing nucleosynthesis processes are active in the galaxy. ^{60}Fe ions have also been detected in galactic cosmic rays with the CRIS/ACE spectrometer [4]. The detection of ^{60}Fe, first in deep-sea ferromanganese crust and marine sediment [5–7], and recently in lunar samples [8], indicates the recent interaction (∼2.2 Myr) of our solar system with the ejecta of one or several nearby ($d < 1$ kpc) supernova explosions, most probably from the Scorpius-Centaurus association [9]. Eventually ^{60}Fe was also observed in presolar grains as an excess of ^{60}Ni [10,11] and understanding the amount and origin of ^{60}Fe can provide valuable information concerning the stellar environment of the nascent solar system.

A common aspect of all these observations is to find the stellar source(s) of ^{60}Fe and the need for accurate nuclear reaction rates concerning ^{60}Fe nucleosynthesis. This isotope is mostly produced in neutron rich environments inside massive stars during convective He and C shell burning [12]. It is synthesized through successive neutron captures on preexisting Fe isotopes during the weak s-process, and its production and destruction are driven by the ^{59}Fe$(n,\gamma)^{60}$Fe and ^{60}Fe$(n,\gamma)^{61}$Fe reactions, respectively.

In the present work, we focus on the study of the ^{60}Fe$(n,\gamma)^{61}$Fe reaction. So far the cross section used in stellar models has been estimated theoretically [13] using the Hauser-Feshbach statistical model. While this only takes into account the resonant component of the cross section, the direct capture can play an important role (or even be dominant as in the case of ^{48}Ca [14]) in the case of a nucleus with low S_n value ($S_n(^{61}\text{Fe}) = 5579$ keV [15]) and when vacant $\ell = 1$ states are present in the $A + 1$ nucleus. The estimation of the direct component requires detailed spectroscopic information of ^{61}Fe states, such as their state energy, associated neutron

*Corresponding author: hammache@ipno.in2p3.fr
†Present address: Department of Physics, University of Surrey, Guildford GU2 5XH, United Kingdom.
‡Present address: Universidade de Santiago de Compostela, E-15786 Santiago, Spain.
§Present address: CEN Bordeaux-Gradignan, F-33175 Gradignan, France.
‖Present address: LPC Caen (IN2P3-CNRS/ISMRA et Université), F-14050 Caen Cedex, France.
¶Present address: KU Leuven, Instituut voor Kern- en Stralingsfysica, B-3001 Leuven, Belgium.
#Present address: CSNSM, IN2P3-CNRS, Université Paris-Sud, 91405 Orsay, France.

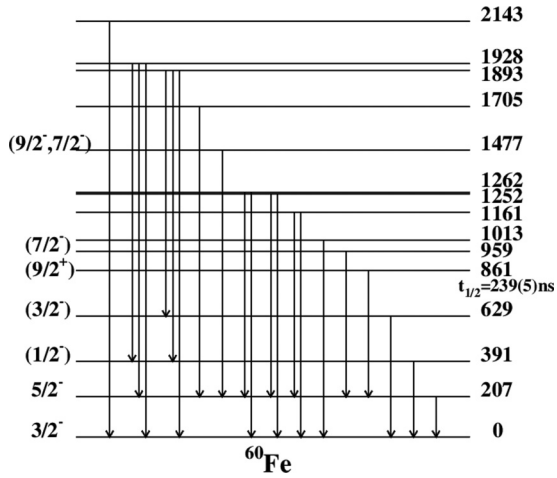

FIG. 1. Experimental ^{61}Fe level scheme below 2.5 MeV adapted from the work of Radulov *et al.* [20]. States are labeled by their excitation energy in keV and spin parity. The γ-ray decays displayed here are those for which branchings are larger than 15%. For more details see Ref. [20].

spectroscopic factor (SF), and orbital momentum ℓ. At the time the present work was started the spectroscopy of ^{61}Fe was rather limited despite several experimental studies populating this nucleus by β decay [16,17], multinucleon transfer [18], or deep inelastic reaction [19]. Few states were known above 1 MeV, and below, the states at 391 and 629 keV had no spin-parity assignments. Recently a detailed measurement of ^{61}Mn β decay [20] improved substantially the ^{61}Fe spectroscopic knowledge with a $(1/2^-)$ tentative assignment for the 391 keV state and $(3/2^-)$ for the 629 keV state. Many new states above 1 MeV were also observed (see Fig. 1) for which γ-ray decay was measured. Nevertheless, none of the identified ^{61}Fe states have measured neutron spectroscopic factors which are needed to evaluate the direct component of the ^{60}Fe$(n,\gamma)^{61}$Fe cross section.

Since the start of the analysis of the present work, a large total cross section for ^{60}Fe$(n,\gamma)^{61}$Fe of 9.9 ± 2.8 (syst) $\pm$ 1.4 (stat) mb was measured through the activation method [21] in which an ^{60}Fe radioactive sample was irradiated by a neutron flux whose energy distribution matched the one expected in massive stars. Such a large cross-section value, twice as large as the Hauser-Feshbach (HF) predicted one, suggests that the resonant capture rate is dominating. Indeed, even if maximum spectroscopic factor values are found for the p states, the direct capture component will contribute for a maximum of 5% to the total cross section. Hence, the present work reports on an experimental study of ^{61}Fe structure (level energy, spin, and SF) with the aim of comparing the results with shell-model calculations for a better modeling of nuclei around $N = 34$ and a better location of the $p_{1/2}$, $g_{9/2}$, and $d_{5/2}$ shells. The spectroscopy of the bound states of ^{61}Fe was studied by means of the neutron transfer reaction ^{60}Fe$(d,p)^{61}$Fe in inverse kinematics.

II. EXPERIMENT

The ^{60}Fe secondary beam was produced at the Grand Accélérateur National d'Ions Lourds (GANIL) by fragmentation

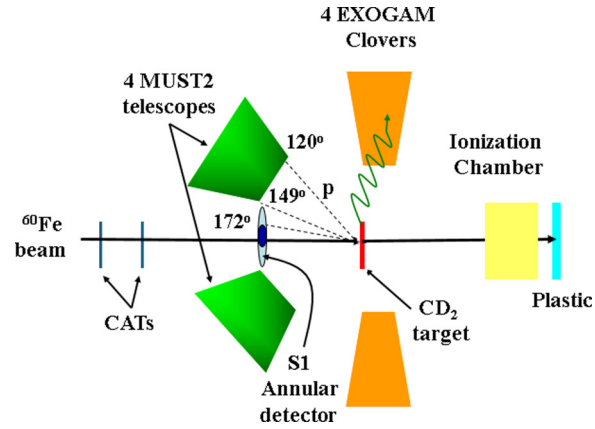

FIG. 2. Schematic view of the experimental setup used to study the ^{60}Fe$(d,p\gamma)^{61}$Fe reaction in inverse kinematics. See text for details.

of a 64.5A MeV ^{64}Ni^{28+} primary beam in a 500 μm ^{9}Be target placed at the entrance of the LISE3 spectrometer [22]. The LISE3 spectrometer was used to select and transport the ^{60}Fe beam which was slowed down using an achromatic 700 μm ^{9}Be degrader between the two dipoles of the spectrometer. A beam of 27A MeV energy and 1×10^5 pps intensity with 55% ^{60}Fe purity was obtained and sent on a 2.6(1) mg/cm^2 deuterated polyethylene (CD_2) target where transfer reactions took place. A purity of 80% relative to the remaining ^{58}Mn and ^{62}Co contaminants was reached after separation of the other beam contaminants ^{61}Fe and ^{64}Ni, using time of flight measurements.

A schematic view of the experimental setup used in this work is shown in Fig. 2. The beam secondary particles were tracked event by event by two position sensitive multiwire proportional chambers (Chambres à Trajectoires de Saclay CATS [23]) placed at 96.2 and 56.2 cm upstream of the CD_2 target. The incident angle of these nuclei and their horizontal by vertical positions at the target were determined with a precision of about 0.12° and 3.3 mm FWHM, respectively.

The protons emitted after beam interaction in the target were detected at backward laboratory angles by two different silicon array systems: the S1 annular double-sided silicon strip detector (DSSSD) from Micron Semiconductor Ltd. and four telescopes of the MUST2 array [24]. The S1 detector, with internal and external diameters of 48 and 96 mm, respectively, has four quadrants of 16 radial strips each and 16 wedge azimuthal strips. Its thickness was 500 μm. The first stage of each MUST2 telescope consists of a square (10×10 cm^2) DSSSD of 300 μm thickness and 128 strips on each side. The second stage is a Si(Li) detector made of 16 pads of 4.5 mm thickness for residual energy measurement. An energy resolution of ≈40–50 keV (FWHM) was determined for the DSSSDs with a 3α source. In case of the Si(Li) detectors the energy resolution was about 80 keV.

Both silicon array systems were placed at ∼15.5 cm from the CD_2 target, covering laboratory angles from 162° to 173° for S1 and from 123° to 159° for MUST2 telescopes. This corresponds to center-of-mass angles of 2.2°–5.7° and 6.7°–21.7°, respectively, when the (d,p) transfer reaction to

the ^{61}Fe ground state is considered. The proton emission angles were obtained with a resolution of about 1.3° (FWHM) in the laboratory frame, from the combination of positions and angles of the beam at the target and the proton position in the silicon arrays (MUST2 and S1).

Identification of the protons was readily achieved by using their energy and time of flight measurements when stopping in the DSSSDs (MUST2 or S1). When punching through the first stage of MUST2 the protons were identified using their energy loss in the DSSSD stage and their residual energy measured in the Si(Li) pads (see Fig. 2 in Ref. [25]).

The emitted γ rays from the deexcitation of the populated states in ^{61}Fe were detected in four segmented Ge detectors from the EXOGAM array [26] placed at 5 cm from the beam axis. The target was shifted 4.2 cm upstream from the center of these detectors in order to optimize the angular coverage of the MUST2 detectors and at the same time to keep a reasonable γ-ray detection efficiency (7% at 1 MeV). The detection of the γ rays is needed to disentangle the different populated states in ^{61}Fe that cannot be discriminated with the charged-particle detection only, because the use of a thick target led to a charge particle resolution of ∼800 keV.

The quasiprojectiles were identified in mass and charge at 0° by measuring their energy loss and time of flight in an ionization chamber followed by a plastic scintillator, respectively.

III. DATA ANALYSIS

The ^{61}Fe excitation energy spectra obtained using the measured proton energy and emission angle are displayed in Fig. 3 for the MUST2 array (top) and the S1 detector (bottom). Two peaked structures below the neutron threshold $S_n = 5579(4)$ keV are clearly observed around 1 and 3 MeV. Each panel of Fig. 3 compares the γ-gated [red (light gray)] and γ-ungated [blue (dark gray)] excitation energy spectrum whatever the γ-ray energy. The γ coincidence ratio at the main broad structure around 1 MeV is much smaller than for the rest of the spectrum. This indicates a strong contribution of the $9/2^+$ isomeric state at 861 keV [$\tau = 239(5)$ ns] for which the associated γ rays are nearly not detected. Indeed, on the one hand, the lifetime of this isomeric state is much larger than the time of flight of ^{61}Fe ions between the target and the plastic where they stop (≃10 ns); on the other hand, the plastic is at a distance of 50 cm from the EXOGAM detectors, which makes the detection efficiency of the isomeric γ rays very low.

Note that no kinematic lines corresponding to the population of ^{69}Mn and ^{63}Co coming from potential (d,p) reactions on the beam contaminant species were observed in the reconstructed proton kinematic lines.

In the following we focus our attention mostly on the first main peak structure around 1 MeV where several states could be identified, with a very short discussion being later dedicated to the second peak around 3 MeV.

Doppler-corrected γ-ray spectra obtained when requiring protons in both S1 and MUST2 detectors are presented in Fig. 4. The chosen excitation energy range covering the first main structure has been split into two subranges of equal 1 MeV width. In the 0.0–1.0 MeV range (black histogram), two

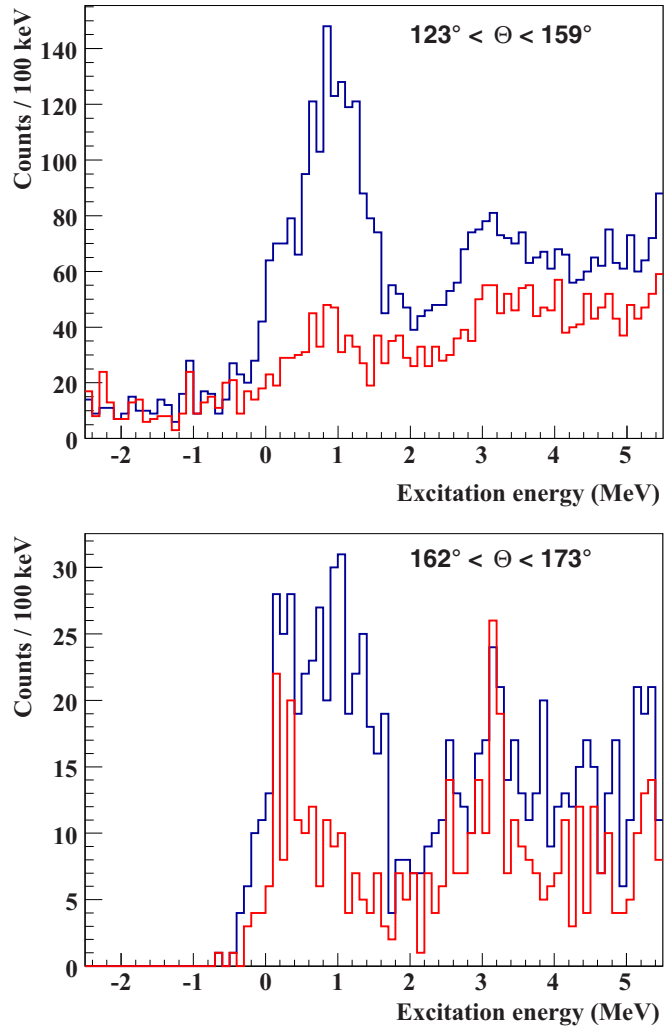

FIG. 3. ^{61}Fe excitation energy spectra obtained with the MUST2 array (top) and the S1 detector (bottom). The blue (dark gray) histograms only rely on protons whereas the red (light gray) histograms additionally require a γ-ray coincidence with EXOGAM; each event is counted as many times as the γ multiplicity, mainly one in the main peak structure. Laboratory angles covered by each charged-particle detector are indicated.

strong γ-ray transitions at 207 and 391 keV are observed with an energy resolution of about 40 keV. No other clear transition is observed on top of a rather important background at higher γ-ray energies. Unfortunately, the origin of this background could not be identified. In the selected excitation energy range, no reported states in the literature [20] cascade with a significant branching through the 391 keV level. Moreover, there is no observation of the 752.6 keV γ-ray transition which would come from the 959 keV state [20] (see Fig. 1) cascading through the 207 keV level with high branching ratio (81%). One can then assert that the two observed transitions come from the direct population of the $f_{5/2}$ state at 207 keV and the $(p_{1/2})$ state at 391 keV.

When the 1.0–2.0 MeV excitation energy range is considered (Fig. 4, red histogram), γ-ray transitions at 207 and 391 keV are still observed but with lower intensity. These

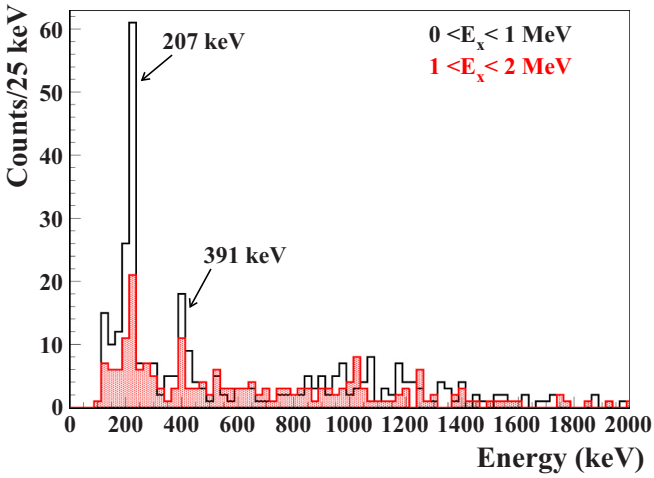

FIG. 4. Doppler-corrected γ-ray energy spectra obtained in coincidence with protons detected in the charged-particle detectors (S1 or MUST2). The black and red shaded histograms correspond to events having an ^{61}Fe excitation energy in the 0.0–1.0 MeV and 1.0–2.0 MeV ranges, respectively.

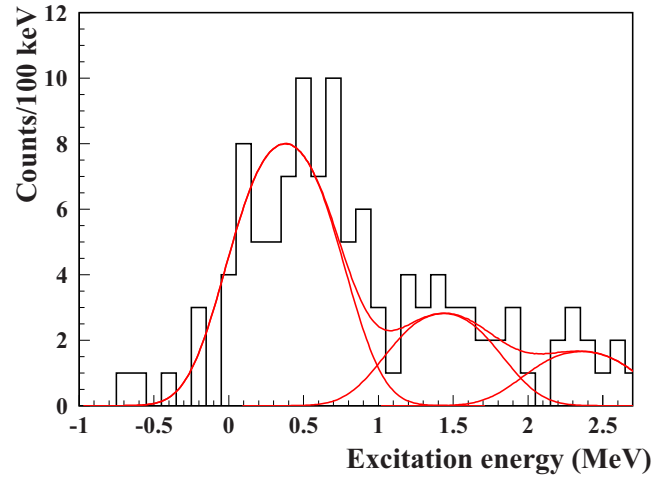

FIG. 5. ^{61}Fe excitation energy spectrum from MUST2 events when gating on the 207 keV γ-ray transition. The red curve is a fit of the spectrum with three components (see text for details).

transitions should come from cascades associated to ^{61}Fe states populated in the considered excitation energy range where actually all states have a component of decay through one of these transitions. In the case of the 391 keV γ-ray transition the state at 1893 keV [20] (see Fig. 1) could be a good candidate. However, a cascade of similar strength to the 629 keV level is not observed, and the decrease of the detection efficiency from 14.8% at 391 keV to 10.5% at 629 keV is not enough to explain this absence. Concerning the 207 keV transition, various states in the selected energy window deexcite through the 207 keV state with relatively high branching ratios [20], e.g., the 1161, 1252, 1263, 1477, 1705, and 1929 keV states. Again no clear and reliable identification of the γ-ray partners could be performed, leading to the conclusion that only a mixture of a weak excitation of these levels is present. Altogether, the identification of the populated states at excitation energies higher than 1 MeV could not be achieved in the present experiment. This is due, on the one hand, to a weak population of these states through the (d,p) reaction together with a spread of the strength over several states and, on the other hand, to the relatively important background observed at γ-ray energies larger than 500 keV together with the decrease of the γ-ray detection efficiency at high energies (22.9% at 207 keV and 6.5% at 1.3 MeV).

The previous discussion can also be complemented by looking at the ^{61}Fe excitation energy spectrum in coincidence with the most intense γ-ray transition at 207 keV. The case of the MUST2 detector is displayed in Fig. 5 where a dominant peak associated to the 207 keV state comes up in the low energy part of the spectrum together with two weaker components more than 1 MeV above. This emphasizes that the γ-ray transition at 207 keV comes mainly from the direct population of the 207 keV state as discussed previously.

The excitation energy spectrum in Fig. 5 was fitted with three components, each described by a template corresponding to the convolution of a gate function accounting for the energy losses of the beam and the emitted protons in the target, and of a Gaussian function encompassing all other experimental effects. The widths of the gate function ($R = 380$ keV) and the Gaussian function ($\sigma = 165$ keV) were obtained from a detailed Monte Carlo simulation using the NPTool package [27]. In the fitting procedure the amplitude and centroid of each template were considered free parameters. An energy shift was then deduced in order to adjust the main peak energy to its known value at 207 keV. Such a shift accounts for systematic effects such as possible errors in the target position as well as in the energy losses in the target or in the DSSSD dead layers. A value of $+170 \pm 65$ keV was found with a $\chi^2/N_{\mathrm{DOF}} = 13.01/23$ (the error on the peak position being transferred to the shift value; N_{DOF} is number of degrees of freedom).

A similar procedure was performed in the case of the ^{61}Fe excitation energy spectrum obtained with the S1 detector and an energy shift of $+100 \pm 70$ keV was obtained ($\chi^2/N_{\mathrm{DOF}} = 5.8/13$).

From the comparison of the Doppler-corrected γ-ray energy spectrum obtained in coincidence with protons detected in MUST2 (blue histogram in Fig. 6) with the one obtained with protons detected in S1 (red histogram in Fig. 6) for the ^{61}Fe excitation energy range from 0 to 1 MeV, one can notice that the population ratio between the two transitions at 207 and 391 keV after efficiency correction is much larger for γs in coincidence with the MUST2 telescope (ratio $= 3.06 \pm 1.16$) than with the S1 detector (ratio $= 1.13 \pm 0.49$). Given that S1 and MUST2 cover different angular ranges, this is a clear indication of different orbital momenta involved for the two states in line with Ref. [20]: $\ell = 3$ for 207 keV and $\ell = (1)$ for 391 keV where the angular distribution is more forward, peaked as shown in Sec. IV.

To extract the proton angular distributions associated with each populated ^{61}Fe state two different procedures were used for the S1 and MUST2 detectors. Such an approach was motivated by the fact that the S1 total counting could be gathered in a single center-of-mass angular bin centered at

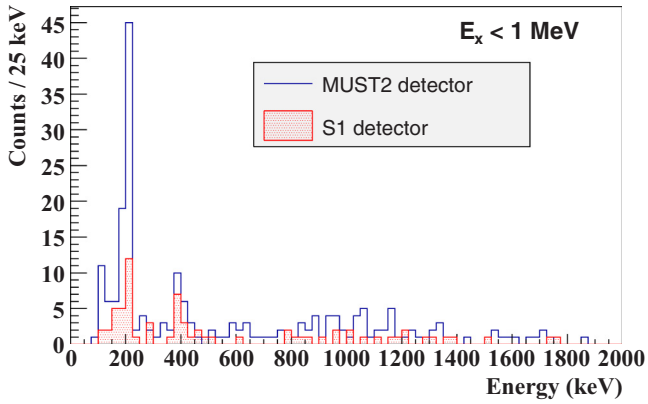

FIG. 6. Comparison of the Doppler-corrected γ-ray energy spectra obtained in coincidence with protons detected in MUST2 (blue histogram) and S1 (red shaded histogram) for ^{61}Fe excitation energy in the 0.0–1.0 MeV range.

$4^\circ \pm 1.3^\circ$ whereas the MUST2 counting could be spread over eight distinct angular bins.

Concerning the S1 detector, the excitation energy spectrum obtained is fitted with five states using a χ^2 minimization procedure (see Fig. 7, top) in order to evaluate the yield of each state. The states are the ground state (g.s.), the three states previously identified at 207, 391, and 861 keV, and an arbitrary state centered at 1600 keV representing a mixture of nonidentified higher states between 1300 and 1900 keV which will not be analyzed. Each state was described by the same template as for the MUST2 case, but with $R = 450$ keV and $\sigma = 170$ keV. The amplitudes of the components associated to the 207 and 391 keV states were constrained with the observed count rates in the 207 and 391 keV γ-ray lines. The best fit shown in Fig. 7 (top) corresponds to $\chi^2/N_{\mathrm{DOF}} = 61/48 = 1.27$. From the extracted proton yield, the ^{2}H(^{60}Fe, p)^{61}Fe differential cross sections corresponding to the g.s. and 207, 391, and 861 keV states were deduced at the mean angle of 4° in the center-of-mass system.

For MUST2 data, the same five states are represented in the angle integrated excitation energy spectrum (blue histogram) displayed in Fig. 7 (bottom), together with a linear background extrapolated from the negative excitation energy part of the spectrum, due to reactions on the carbon present in the CD_2 target. Once spread over eight angular bins, the obtained statistic is no longer large enough to easily use a fitting method to derive the proton yields at each angle for each state as in the case of the S1 analysis. A matrix method (see Appendix A) is then used to extract the differential cross sections for eight angular bins after background subtraction. Because of the low statistics and the large overlap between the three first states (g.s., 207 keV, and 391 keV), a 3×3 matrix procedure was applied only on the dominant peaks at 207, 891, and 1600 keV. Different sets of width and center of the three excitation energy ranges considered in the matrix procedure were used in order to check the reliability of the analysis and to estimate the errors attached to the resulting angular distributions. Because of the proximity of the 207 keV state with the ground and 391 keV states, the result for the 207 keV state is mixed with a rather large part of its neighbors. This contribution factor is

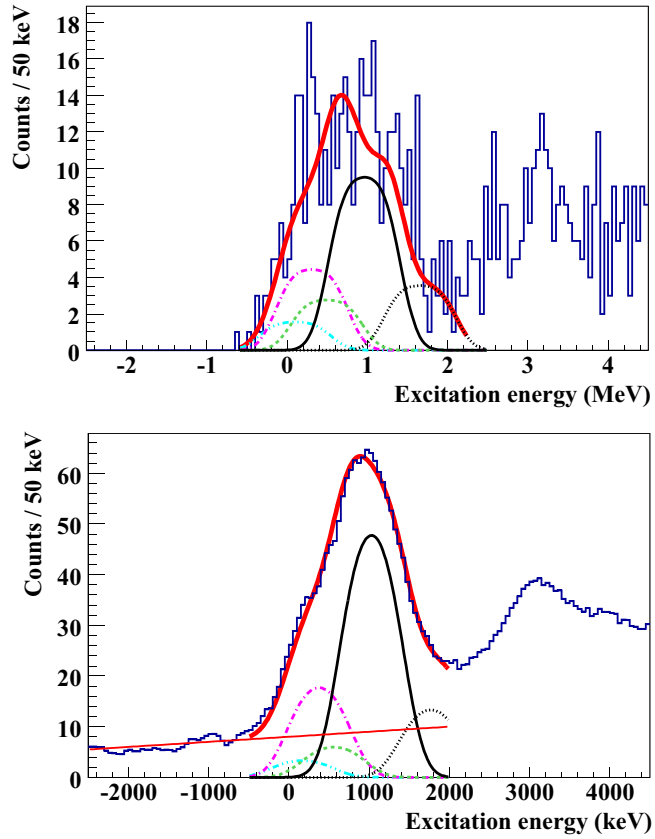

FIG. 7. Top: Fit of the ^{61}Fe excitation energy spectrum (S1 detector) with the g.s. and 207, 391, and 861 keV states and a higher state centered at 1600 keV. Bottom: ^{61}Fe excitation energy spectrum for MUST2 array with the contribution of the same set of ^{61}Fe states. The red linear curve corresponds to the carbon background. The turquoise dash-double-dotted, pink dash-dotted, green dashed, black solid, and black dotted curves correspond to the g.s. and the 207, 391, 861, and 1600 keV states, respectively. The red thick solid curve corresponds to the sum.

evaluated within the matrix analysis at 83% (see Appendix B) for the used energy range of 400 keV width and an energy separation of $\simeq$200 keV for the two neighboring states.

In Fig. 7 (bottom), the contributions coming from the five considered ^{61}Fe states are drawn. The used amplitudes come from the 3×3 matrix, the S1 results, and the adiabatic distorted wave approximation (ADWA) analysis described below. One can observe that the sum of these contributions (red curve) describes correctly the experimental histogram and that the ground and 391 keV states have small relative contributions, smaller even than for S1.

IV. RESULTS

Figures 8(a) and 8(b) display the differential cross sections extracted for the excitation energy range (7–407 keV) centered at 207 keV where a contribution of the $p_{3/2}$ ground state and the ($p_{1/2}$) 391 keV state is present, and for the 861 keV state ($J^\pi = 9/2^+$), respectively. The black circles are differential cross sections extracted from MUST2 data using the matrix method while the red square corresponds to the extracted cross

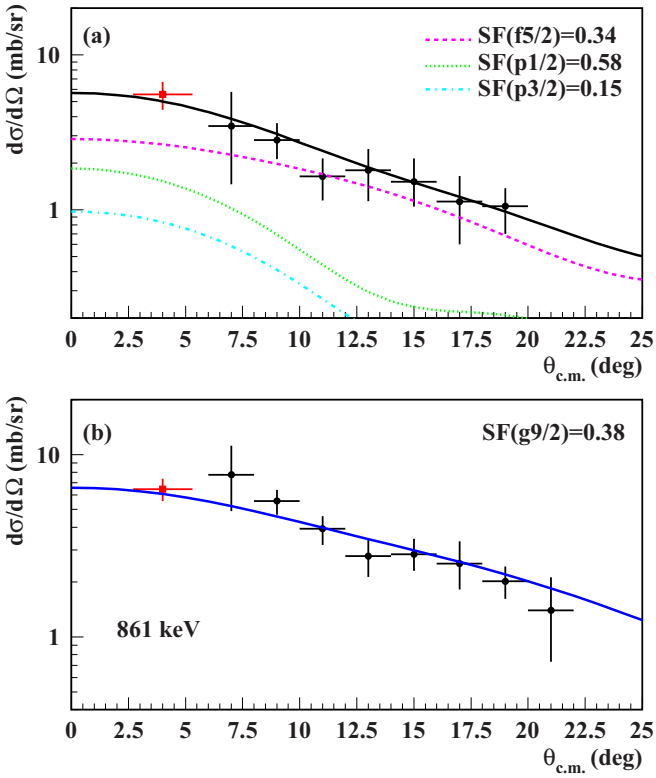

FIG. 8. Experimental proton angular distributions for (a) the excitation energy range corresponding to the 207 keV state and (b) the 861 keV excited state, together with zero-range ADWA calculations normalized to the data. The black solid line in (a) corresponds to a combination of calculations with $\ell = 3$ for the $f_{5/2}$ 207 keV state (pink dashed curve) and $\ell = 1$ for the $(p_{1/2})$ 391 keV (green dotted curve) and the $p_{3/2}$ gs (turquoise dash-dotted curve) states. The blue solid line in (b) corresponds to calculation with $\ell = 4$ for the $g_{9/2}$ 861 keV state.

sections at 4° using the fit procedure of the S1 excitation energy spectrum. The error bars assigned to the measured differential cross sections include the uncertainties on the extracted yield, the number of target atoms, the solid angle, and the integrated charge. Because the MUST2 data in Fig. 8(a) include contributions from the ground state and the 391 keV state, the S1 data point at 4° is the sum of the extracted cross section for the 207 keV state (3.16 ± 0.63 mb/sr) and those for the ground state (1.0 ± 0.5 mb/sr) and the 391 keV state (1.82 ± 0.64 mb/sr) weighted with the factor 83% determined from the 3×3 matrix procedure (see above).

ADWA calculations [28] were performed with the FRESCO code [29] using global optical potentials for the entrance [30] and exit [31] channels of the (d,p) reaction. Concerning the form factor, standard values for the radius ($r_0 = 1.25$ fm) and diffuseness ($a_0 = 0.65$ fm) were used for the $p + {}^{60}$Fe Woods-Saxon potential. The depth of this potential was adjusted to reproduce the binding energy of each considered ^{61}Fe state.

The experimental differential cross sections displayed in Fig. 8(a) are fitted using a combination of an $\ell = 3$ ($E_x = 207$ keV, $f_{5/2}$) component, an $\ell = 1$ ($E_x = 391$ keV, $p_{1/2}$) component as tentatively assigned by Ref. [20], and an $\ell = 1$ component corresponding to the $p_{3/2}$ ground state.

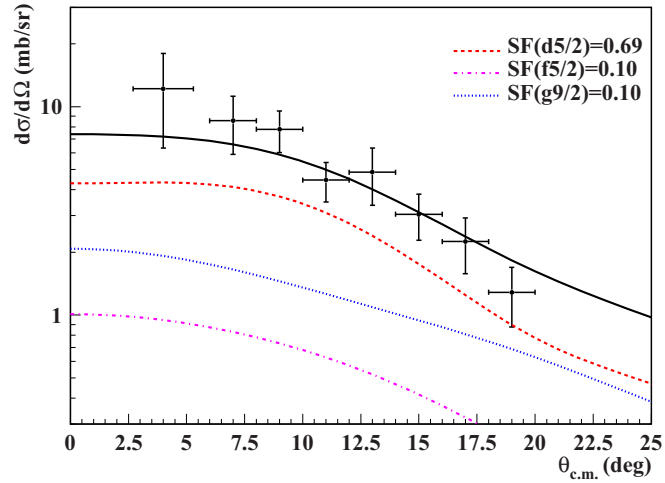

FIG. 9. Experimental proton angular distributions for the whole excitation energy range between 2.0 and 4.0 MeV, together with zero-range ADWA calculations normalized to the data. The black solid line corresponds to an optimized combination of an $\ell = 2$ for $d_{5/2}$ (red dashed curve), $\ell = 3$ for $f_{5/2}$ (pink dashed-dotted curve), and $\ell = 4$ for $g_{9/2}$ (blue dotted curve).

The spectroscopic factors of the g.s. and the 391 keV states were fixed to the values determined from the normalization of the ADWA calculations to the single extracted data point from the S1 telescope, which are $\mathrm{SF}(p_{1/2}) = 0.58 \pm 0.20$ and $\mathrm{SF}(p_{3/2}) = 0.15 \pm 0.06$. Both these components are weighted in the fitting procedure with the factor of 83% mentioned earlier.

As a result, the SF of the 207 keV state was found to be 0.34 ± 0.10 with the best χ^2 fit shown in Fig. 8 ($\chi^2_\nu = 0.5$). The ratio of integrated ADWA cross sections for the 207 and 391 keV states over the MUST2 and S1 angular range gives 3.1 ± 1.4 and 1.45 ± 0.65, respectively. This is consistent with what we deduced from the analysis of the γ-ray spectra in Fig. 6. Hence, this work establishes the $\ell = 1$ nature of the 391 keV state, in agreement with the tentative assignment of Ref. [20].

A SF of 0.38 ± 0.07 for the 861 keV ($J^\pi = 9/2^+$), with a $\chi^2_\nu = 0.47$, was obtained from the best χ^2 fit of the angular distribution displayed in Fig. 8(b) with an $\ell = 4$ component.

In the 2.0–4.0 MeV excitation energy range where a second large peak structure is observed, no states could be identified. However, an angular distribution corresponding to the whole peak was deduced and analyzed using ADWA calculations (see Fig. 9). The deduced experimental differential cross sections are fitted using a combination of an $\ell = 2$ ($d_{5/2}$), $\ell = 3$ ($f_{5/2}$), and $\ell = 4$ ($g_{9/2}$). From the best fit, SF values of 0.69 ± 0.20, 0.10 ± 0.19, and 0.10 ± 0.05, respectively, were deduced with $\chi^2_\nu = 0.93$.

A comparison of the energies and the corresponding spectroscopic factors deduced in this work with those predicted by shell-model (SM) calculations within an $fpgd$ valence space using the Lenzi-Nowacki-Poves-Sieja (LNPS) effective interaction [32] is given in Fig. 10. A very good agreement is observed, at energies below 1 MeV, between the two sets of spectroscopic factors within their error bars. In this work, the

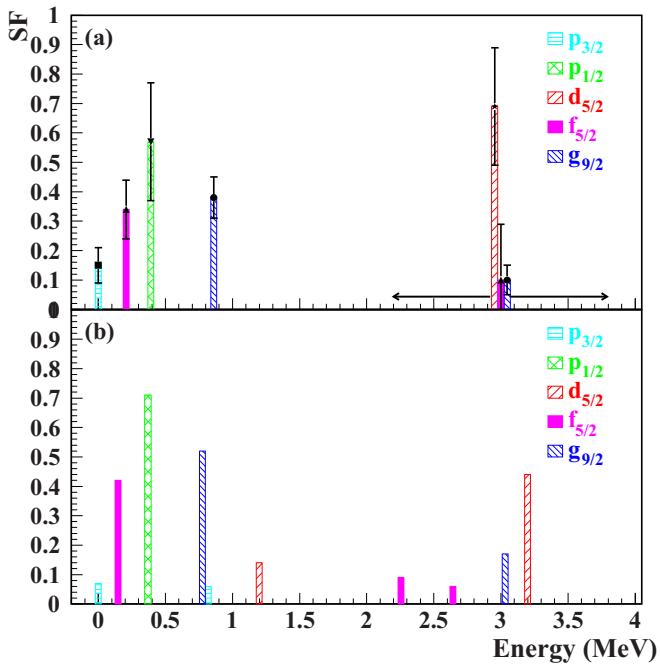

FIG. 10. (a) Experimental SFs obtained in this work with their error bars. (b) Predicted SF from shell-model calculation (see text). The turquoise, green, red, pink, and blue boxes correspond to $p_{3/2}$, $p_{1/2}$, $d_{5/2}$, $f_{5/2}$, and $g_{9/2}$ orbitals, respectively. The arrow indicates the energy range that corresponds to the displayed spectroscopic factors in the second peak structure.

presence of a $d_{5/2}$ state with a large SF in the energy range 2.0–4.0 MeV is found in agreement with the predictions of the shell-model calculation. However, the exact location of this state within this energy range could not be determined in this work.

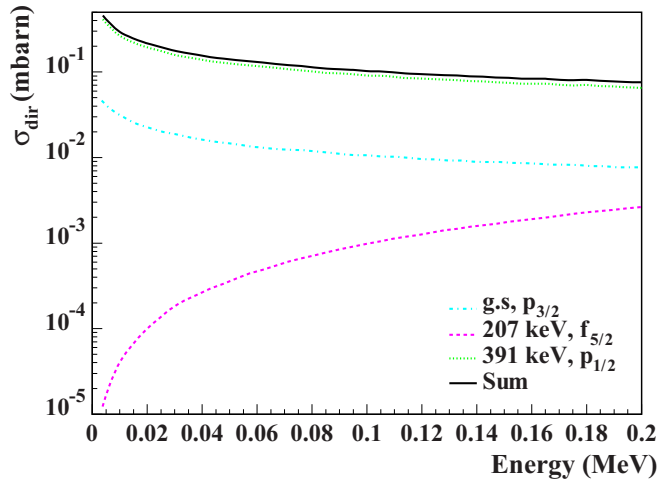

FIG. 11. Direct capture cross section of the ^{60}Fe$(n,\gamma)^{61}$Fe reaction with the TEDCA code. The turquoise dash-dotted, pink dashed, and green dotted curves correspond to calculations of the $p_{3/2}$ ground state, $f_{5/2}$ first excited state, and $p_{1/2}$ second excited state, respectively. The black solid curve is the sum of the three contributions.

The good agreement between the spectroscopic factors deduced in this work and the SM predictions confirms further the reliability of the present shell-model calculations in the region around $N = 34$.

Calculations of the direct capture cross section of the ^{60}Fe$(n,\gamma)^{61}$Fe reaction, dominated by $\ell = 1$ to a large extent, were performed using the TEDCA code [33] and our deduced neutron spectroscopic factors for the $p_{3/2}$ ground state (SF = 0.15), $f_{5/2}$ first excited state (SF = 0.34), and $p_{1/2}$ second excited state (SF = 0.58) of ^{61}Fe, which correspond to the p-wave and the negligible f-wave neutron capture. They are displayed in Fig. 11. At the energy where the ^{60}Fe$(n,\gamma)^{61}$Fe reaction occurs in massive stars, namely, 25 keV, the direct capture cross section is found to be 0.20 ± 0.07 mb. This value represents only 2% of the total ^{60}Fe$(n,\gamma)^{61}$Fe cross section deduced from the activation measurement of Uberseder *et al.* [21] and indicates that the resonant component is dominating.

V. CONCLUSION

In summary, the spectroscopy of ^{61}Fe was investigated through the one neutron transfer reaction ^{60}Fe$(d,p\gamma)^{61}$Fe in inverse kinematics at 27A MeV incident energy. For the first time, the neutron spectroscopic factors of the g.s., $J^\pi = 3/2^-$; 207 keV state, $J^\pi = 5/2^-$; 391 keV state, $J^\pi = 1/2^-$, and 861 keV state, $J^\pi = 9/2^+$, were determined experimentally from an ADWA analysis of the data. This work establishes as well the $\ell = 1$ nature of the 391 keV state. The deduced spectroscopic factors were found in very good agreement with those predicted by shell-model calculations. This confirms further the reliability of the present shell-model calculations in this region of nuclei. The calculated direct component of the ^{60}Fe$(n,\gamma)^{61}$Fe cross section was found of about 2% of the total, indicating a dominant resonant neutron capture component.

ACKNOWLEDGMENTS

We would like to thank the IPN and GANIL technical staff, particularly Emmanuel Rindel, Patrice Gangnant, and Jean-François Libin, for their strong support during the preparation and running of the experiment.

APPENDIX A: MATRIX METHOD USED TO EXTRACT STATE PEAK YIELDS FROM A SPECTRUM OF OVERLAPPING PEAKS

A method is presented as an alternative to a fitting procedure when numerous spectra with the same states have to be analyzed as it happens when studying angular distributions. As in a fitting procedure a precise knowledge of the peak shape is a prerequisite. A combination of two error functions were used in the article (convolution of a Gaussian and a step function) but for simplicity a Gaussian is used in the example presented below and in Fig. 12. Note that statistics has to be enough for getting peak yields (total number of counts in the peak) of the smaller peaks or for separating one peak from its too closely overlapping neighbor.

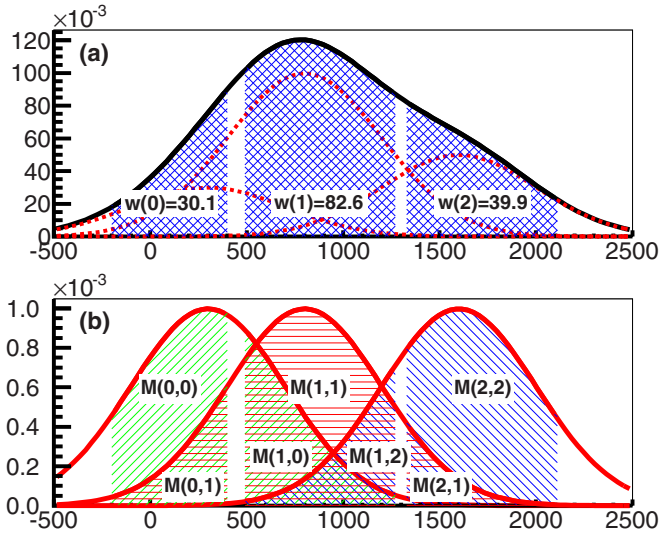

FIG. 12. Three states at 200, 800, and 1600 keV are contributing with a peak yield of 30, 100, and 50 to the spectrum displayed in (a). The corresponding countings within the three chosen ranges are 30, 83, and 40. The elements of a matrix **M** are constructed (see text) as illustrated in (b). The inverted matrix $\mathbf{M}^{-1}$ is used to calculate the initial peak yields from the observed range countings.

Though it could be applied to any number of overlapping peaks, it is presented here with three peaks as required in this article.

Let us consider three states **E1**, **E2**, and **E3** [Fig. 12(a)], each with an unknown peak yield $v1$, $v2$, and $v3$ (thin dotted red line) to an observed spectrum (thick black line). A counting range R_i (blue hatched area) is associated with each states from $E_{\mathrm{inf}\,i}$ to $E_{\mathrm{sup}\,i}$. Within these ranges w_i counts are found which are the three components of a three-dimensional vector **w**. The ranges are chosen in order to optimize the contribution of their associated peak, taking into account that each range comprises a given fraction of the E_j peak but also a fraction of the two other overlapping (neighboring or not) peaks. The mixed contributions w_i result from a linear combination of the three (unknown) peak yields v_j.

This linear dependence is represented by a 3×3 matrix **M** whose elements m_{ij} are given by

$$m_{ij} = \int_{E_{\mathrm{inf}\,i}}^{E_{\mathrm{sup}\,i}} \mathrm{Gauss}(E_j)\, dE, \tag{A1}$$

where $\mathrm{Gauss}(E_j)$ is the normalized Gaussian function centered on E_j. This is illustrated in Fig. 12(b).

More precisely the matrix **M** relates the vector **w** of the three countings in the three ranges to the vector **v** of the peak yields through

$$\mathbf{w} = \mathbf{M} \times \mathbf{v}. \tag{A2}$$

Once this relation is inverted, the sought vector **v** is now related to the observed countings **w** through

$$\mathbf{v} = \mathbf{M}^{-1} \times \mathbf{w}. \tag{A3}$$

The uncertainties on the v components are given by

$$\delta v_i = \sqrt{\sum_j \left(M^{-1}_{i,j}\right)^2 \times w_j}. \tag{A4}$$

A numerical example illustrated with Fig. 12 is given below.

Let us consider that the unknown peak yields are $\mathbf{v} = (30,100,50)$ and that the observed range countings are $\mathbf{w} = (30.1,82.6,39.9)$.

The calculated matrix elements and the inverted ones are then found to be

$$\mathbf{M} = \begin{pmatrix} 0.4931 & 0.1524 & 0.001347 \\ 0.2998 & 0.6431 & 0.1878 \\ 0.004329 & 0.08399 & 0.6284 \end{pmatrix}$$

and

$$\mathbf{M}^{-1} = \begin{pmatrix} 2.384 & -0.5873 & 0.1704 \\ -1.151 & 1.902 & -0.566 \\ 0.1375 & -0.2502 & 1.666 \end{pmatrix}.$$

By applying Eq. (5), one finds the peak yields $\mathbf{v} = (30,100,50)$, as expected.

APPENDIX B: CASE OF WEAKLY POPULATED CLOSE SATELLITE PEAKS

We now consider the more complex case of the ^{61}Fe spectrum discussed in the main body of the article where five states e1 to e5 are identified at 0, 207, 391, 861, and 1600 keV, respectively. The three dominating states are e2, e4, and e5 and the weakly populated states e1 and e3 are close satellites of the locally dominating e2. In this situation, a simple five-state matrix calculation would require more statistics and instead the three-state matrix calculation described previously is used with the triplet of states e1, e2, and e3 treated as a single state with the matrix parameters of the dominating state e2.

For the sake of writing simplicity and to follow the procedure described in the first part of this appendix, let us identify e2 as E1, e4 as E2, and e5 as E3 for a 3×3 matrix calculation.

Because the satellites e1 and e3 are assumed to be weakly populated and are so, they do not affect the results for E2 and E3. However, because the satellites e1 and e3 are ignored in the 3×3 matrix calculation, the result for E1 will include not only the expected true contribution of E1 but also a contribution of its close satellites e1 and e3 whose contributing fraction is calculated as follows.

From equation (A1), the fraction of E1 found within its counting range R_1 is

$$F^{\mathrm{E1\equiv e2}} \equiv m_{11} = \int_{E_{\mathrm{inf}\,1}}^{E_{\mathrm{sup}\,1}} \mathrm{Gauss}(E_1)\, dE.$$

The fraction of e1 and e3 found within the same E1 counting range is

$$F^{\mathrm{e1}} = \int_{E_{\mathrm{inf}\,1}}^{E_{\mathrm{sup}\,1}} \mathrm{Gauss}(e_1)\, dE \quad \text{and} \quad F^{\mathrm{e3}} = \int_{E_{\mathrm{inf}\,1}}^{E_{\mathrm{sup}\,1}} \mathrm{Gauss}(e_3)\, dE,$$

where E1 is replaced by e1 or e3 while keeping the same integral limits.

The ratio $r1 = F^{e1}/F^{E1\equiv e2}$ gives the fraction of e1 mixed with $E1 \equiv e2$ and similarly for $r3 = F^{e3}/F^{E1\equiv e2}$ for the fraction of e3.

For the case treated in the main body of the article (with a different peak shape) and because the two satellite peaks at 0 and 391 keV are equally ∼200 keV distant from the dominant peak at 207 keV, the same fraction of 83% is found with the used range width of 400 keV for both satellites. A fraction of 83% seems important but it turns out to be a small contribution since the satellites are weakly populated.

[1] G. Rugel, T. Faestermann, K. Knie, G. Korschinek, M. Poutivtsev, D. Schumann, N. Kivel, I. Gunther-Leopold, R. Weinreich, and M. Wohlmuther, Phys. Rev. Lett. **103**, 072502 (2009).

[2] D. M. Smith *et al.*, New Astron. Rev. **48**, 87 (2004).

[3] W. Wang *et al.*, Astron. Astrophys. **469**, 1005 (2007).

[4] W. R. Binns *et al.*, Science **352**, 677 (2016).

[5] K. Knie, G. Korschinek, T. Faestermann, E. A. Dorfi, G. Rugel, and A. Wallner, Phys. Rev. Lett. **93**, 171103 (2004).

[6] C. Fitoussi, G. M. Raisbeck, K. Knie, G. Korschinek, T. Faestermann, S. Goriely, D. Lunney, M. Poutivtsev, G. Rugel, C. Waelbroeck, and A. Wallner, Phys. Rev. Lett. **101**, 121101 (2008).

[7] A. Wallner *et al.*, Nature (London) **532**, 69 (2016).

[8] L. Fimiani, D. L. Cook, T. Faestermann, J. M. Gomez-Guzman, K. Hain, G. Herzog, K. Knie, G. Korschinek, P. Ludwig, J. Park, R. C. Reedy, and G. Rugel, Phys. Rev. Lett. **116**, 151104 (2016).

[9] D. Breitschwerdt *et al.*, Nature (London) **532**, 73 (2016).

[10] S. Mostefaoui *et al.*, New Astron. Rev. **48**, 155 (2004).

[11] H. Tang and N. Dauphas, Earth Planet. Sci. Lett. **359-360**, 248 (2012).

[12] M. Limongi and A. Chieffi, Astrophys. J. **647**, 483 (2006).

[13] T. Rauscher and F.-K. Thielemann, At. Data Nucl. Data Tables **75**, 1 (2000).

[14] E. Krausmann, W. Balogh, H. Oberhummer, T. Rauscher, K. L. Kratz, and W. Ziegert, Phys. Rev. C **53**, 469 (1996).

[15] http://www.nndc.bnl.gov/chart/

[16] E. Runt *et al.*, Nucl. Phys. A **441**, 237 (1985).

[17] R. Grzywacz, R. Beraud, C. Borcea, A. Emsallem, M. Glogowski, H. Grawe, D. Guillemaud-Mueller, M. Hjorth-Jensen, M. Houry, M. Lewitowicz, A. C. Mueller, A. Nowak, A. Plochocki, M. Pfutzner, K. Rykaczewski, M. G. Saint-Laurent, J. E. Sauvestre, M. Schaefer, O. Sorlin, J. Szerypo, W. Trinder, S. Viteritti, and J. Winfield, Phys. Rev. Lett. **81**, 766 (1998).

[18] S. Lunardi, S. M. Lenzi, F. Della Vedova, E. Farnea, A. Gadea, N. Marginean, D. Bazzacco, S. Beghini, P. G. Bizzeti, A. M. Bizzeti-Sona, D. Bucurescu, L. Corradi, A. N. Deacon, G. de Angelis, E. Fioretto, S. J. Freeman, M. Ionescu-Bujor, A. Iordachescu, P. Mason, D. Mengoni, G. Montagnoli, D. R. Napoli, F. Nowacki, R. Orlandi, G. Pollarolo, F. Recchia, F. Scarlassara, J. F. Smith, A. M. Stefanini, S. Szilner, C. A. Ur, J. J. Valiente-Dobon, and B. J. Varley, Phys. Rev. C **76**, 034303 (2007).

[19] N. Hoteling, W. B. Walters, R. V. F. Janssens, R. Broda, M. P. Carpenter, B. Fornal, A. A. Hecht, M. Hjorth-Jensen, W. Krolas, T. Lauritsen, T. Pawlat, D. Seweryniak, J. R. Stone, X. Wang, A. Wohr, J. Wrzesinski, and S. Zhu, Phys. Rev. C **77**, 044314 (2008).

[20] D. Radulov, C. J. Chiara, I. G. Darby, H. De Witte, J. Diriken, D. V. Fedorov, V. N. Fedosseev, L. M. Fraile, M. Huyse, U. Köster, B. A. Marsh, D. Pauwels, L. Popescu, M. D. Seliverstov, A. M. Sjödin, P. Van den Bergh, P. Van Duppen, M. Venhart, W. B. Walters, and K. Wimmer, Phys. Rev. C **88**, 014307 (2013).

[21] E. Uberseder, R. Reifarth, D. Schumann, I. Dillmann, C. Domingo Pardo, J. Görres, M. Heil, F. Käppeler, J. Margamiec, J. Neuhausen, M. Pignatari, F. Voss, S. Walter, and M. Wiescher, Phys. Rev. Lett. **102**, 151101 (2009).

[22] R. Anne *et al.*, Nucl. Instrum. Methods Phys. Res. Sect. B **70**, 276 (1992).

[23] S. Ottini *et al.*, Nucl. Instrum. Methods Phys. Res. Sect. A **431**, 476 (1999).

[24] E. Pollacco *et al.*, Eur. Phys. J. A **25**, 287 (2005).

[25] S. Giron *et al.*, *Proceedings of the 11th Symposium on Nuclei in the Cosmos (NIC XI), Heidelberg, Germany, 19-23 July 2010* (Proceedings of Science, 2010), p. 190.

[26] S. L. Shepherd *et al.*, Nucl. Instrum. Methods Phys. Res. Sect. A **434**, 373 (1999).

[27] A. Matta *et al.*, J. Phys. G: Nucl. Part. Phys. **43**, 045113 (2016).

[28] R. C. Johnson and P. C. Tandy, Nucl. Phys. A **235**, 56 (1974).

[29] I. J. Thompson *et al.*, Comput. Phys. Rep. **7**, 167 (1988).

[30] G. L. Wales and R. C. Johnson, Nucl. Phys. A **274**, 168 (1976).

[31] R. L. Varner, Phys. Rep. **201**, 57 (1991).

[32] S. M. Lenzi, F. Nowacki, A. Poves, and K. Sieja, Phys. Rev. C **82**, 054301 (2010).

[33] H. Krauss, Computer code TEDCA (1995).